A morphological investigation of electrodes for solid electrolytes

J. D. CANADAY, T. A. WHEAT
Ceramic Section, Mineral Sciences Laboratory, CANMET, Department of Energy, Mines and Resources Canada, 555 Booth Street, Ottawa, Ontario, Canada K1A 0G1

M. P. HALEY
Westroc Industries Limited, 2424 Lakeshore Road West, Mississauga, Ontario, Canada L5J 1K4

I. H. JOYCE
Ontario Research Foundation Sheridan Park Research Community, Mississauga, Ontario, Canada L5K 1B3

Using the techniques of image analysis, profilometry, gas permeability, mercury porosimetry, and gas adsorption, the morphological properties of porous electrode film (1 to 300 μm) materials are discussed. The materials include platinum paste which is utilized as electrodes for high-temperature oxygen-ion-conducting ZrO_2 electrolytes and for low-temperature solid-state protonic electrolytes. Also considered are plasma-sprayed nickel layers and silver membranes. It is shown that each of the five methods can be used to make quantitative evaluations of film electrodes. The electrode morphological parameters measured include particle diameter, pore diameter, porosity, three-phase line, thickness, surface texture, gas-flow/pressure, pore area, and surface area. A discussion of these properties as they relate to activation and concentration polarization of electrochemical cells is also presented.

1. Introduction

The morphology of the electrodes used in certain types of electrochemical cells has been known [1–9] to affect the performance of these devices. Of particular interest here is the three-phase cell consisting of a solid (ceramic) electrolyte (in which mobile ionic species migrate or diffuse), porous metal electrodes and reactant gas species. This structure may be compared with two-phase electrochemical cells containing a liquid or solid electrolyte and non-porous metal electrodes.

A number of three-phase cells has been under intensive study. The cell with doped ZrO_2 [1–9] as the electrolyte is an anionic conductor, having O^{2-} ions as the mobile species. The operating temperatures of this cell is 800 to 1000° C. A cationically conducting cell based on the $SrCeO_3$ electrolyte [10–13] also operates in this temperature range and has protons as its mobile species.

Two protonic conductors which operate at 25 to 300° C have also been developed. The β/β''-Al_2O_3 [14–16] and Nasicon [17, 18] formulations show promise as precursor electrolytes for fuel cells, electrolysers and sensors. In order for these materials to be used in hydrogen cells, it is necessary for the mobile cationic species to be exchanged for hydronium, H_3O^+, ions. A method for ion-exchanging the precursor material in powder form and then bonding the exchanged powder with an inorganic substance has been developed [19].

A number of electrochemical devices have been reported which utilize the hydronium electrolyte; reviews of cell components and device applications are available [20–22]. The use of the Nasicon electrolyte in a hydrogen sensor and a hydrogen pump [23] has been shown. As a sensor, the Nernstian behaviour was approximated, and when operated as a pump, a current density of 10 mA cm^{-2} was obtained at 30 V. Additional studies of hydrogen electrolysis have been made [24] in which a current of 200 mA passed and where the electrolysis proceeded with an efficiency of 100%. When operated as a fuel cell [25], an open circuit voltage of 0.8 V and a maximum current density of 0.3 mA were obtained. The water-electrolysis and fuel-cell characteristics of the H_3O^+ β/β''-Al_2O_3 cell have also been described [26].

The interrelationships between electrode morphology and polarization mechanism have been discussed and summarized for the Pt/ZrO_2 system [7]. In this study, a number of very different morphologies were considered; they included porous paste, non-porous foil, sputtered electrodes and point electrodes. For the temperature range, oxygen pressure, and current density associated with each of these morphologies, the rate-limiting or polarization mechanisms were discussed. A more recent investigation [27] considered the effects of temperature, film thickness and gas atmosphere on the surface area, particle size, and three-phase-line length of sputtered platinum electrodes.

Investigations of morphology–polarization effects have been made with platinum paste and sputtered platinum as the most common electrode materials. At

0022–2461/89 $03.00 + .12

high oxygen pressures, the current over-potential curves were found to obey the Butler–Volmer equation which implied a charge transfer (or activation) polarization [28]. Also in this study, it was found that at low oxygen pressure, a limiting-current behaviour resulted which was characteristic of cathodic concentration polarization. Similar conclusions were reached [29] regarding the effect of oxygen pressure in an analysis which contained measurements of the two-phase contact area and the length of the three-phase line. In an additional study [30], a model was proposed in which a fraction of the oxygen molecules arriving at the three-phase line is ionized directly and enters the electrolyte and a second part diffuses as oxygen atoms along the two-phase interface before being ionized. Recently, some of the previous results [29], have been reinterpreted in view of newer models and experiments [8, 9]. It was claimed that charge-transfer kinetics cannot be the rate-determining step of the electrode reaction even at high oxygen pressure. Rather, the reaction proceeds by the surface diffusion of adsorbed oxygen atoms on platinum and by the dissociative adsorption of oxygen gas molecules near the three-phase line.

In this investigation, the need for film characterization has been driven by the demand in the electrochemical sciences to understand better the dependence of physical morphology on the operational behaviour of porous electrodes. The efficiency of these devices can be limited by the physical structure of the electrode. The development of suitable characterization techniques will obviously lead to better control of the morphology of formed electrodes, resulting in a means to evaluate alternative electrode compositions. This result will have the potential effect of increasing device efficiency while improving overall cell viability (i.e. material cost, assembly methods, lifetime and reliability).

The objective of this study, therefore, was to identify, develop, refine, and implement characterization techniques which will quantitatively determine the physical structure of electrode film materials in a reliable and reproducible manner. Five techniques were utilized to measure the properties of electrode materials; they are image analysis, profilometry, gas permeability, mercury porosimetry, and gas adsorption.

2. Morphological parameters and electrochemical processes

2.1. Morphological parameters

A schematic diagram of a solid-electrolyte cell is shown in Fig. 1a. An obviously important feature of an electrode is its thickness. The distinction between thin films and thick films, when seen in the context of solid-state devices, is somewhat arbitrary. The former may be considered to have a thickness of less than 1 μm. Electrodes in this category are often deposited by the sputtering process. Thick-film electrodes, with thicknesses of 1 to 100 μm, can be deposited as pastes or by the plasma-spray method. With porous electrodes, the pore diameter, particle diameter, per cent porosity, and the surface area can also be measured. At the interface between an electrode particle and the electrolyte substrate is the two-phase contact area which is shown in Fig. 1b. The perimeter of this region is known as the three-phase line where the electrode, electrolyte, and reactant gas phases are in mutual contact.

In electrochemical terms [31], the three-phase system can be considered as two distinctive catalytic regions. One region is the gas–platinum interface where the reactant gas species is adsorbed on the surface of the electrode platinum particles. Here, chemical reactions such as dissociation, $H_2 \leftrightharpoons 2H$ or $O_2 \leftrightharpoons 2O$, occur. In this two-phase region, platinum is acting as a heterogeneous catalyst. The second region is the interface between the platinum and the electrolyte where the electrode particle is acting as an electrocatalyst. Here, ions within the electrolyte, when reaching the interface, participate in charge transfer or reduction–oxidation (redox) reactions. Presumably, along the three-phase perimeter of the platinum particles, both types of catalytic processes occur. A model of these processes has been developed [30] for the reduction of oxygen in the Pt/ZrO_2 system. From a visualization of these concepts, it is evident that lower electrical currents will occur when the electrode is a continuous (non-porous) foil rather than a porous structure. This result has been demonstrated [32] for the Pt/ZrO_2 cell.

2.2. Electrochemical processes

For a two-phase, metal-electrode/liquid-electrolyte system, the general equation [33] for the molar flux of a species in one dimension is

$$J = Cv - D\frac{dC}{dx} - \frac{ZF}{RT}DC\frac{dV}{dx} \quad (1)$$

where the three terms represent convectional, diffusional, and migrational processes, respectively. The concentration of the species is given by C, the linear velocity is v, and the diffusion coefficient is D. The negative signs of the diffusion and migration terms indicate that material and charge are being transported away from the electrode. Faraday's constant, the electric charge, gas constant, and absolute temperature are given by F, Z, R, and T, respectively.

The three-phase system consisting of an ideal reactant gas at a partial pressure, P, a porous metal electrode, and a solid electrolyte can be modelled analogously to the terms of Equation 1 by similar relations, for convection, diffusion, and migration. The convective term for molecular gas flow outside the cell is

$$J_c = \frac{P}{RT}\frac{f}{A} \quad (2)$$

The linear velocity is $v = f/A$ where f is the volumetric flow rate, and A is the cross-sectional area of the electrode. Two diffusive processes may be considered for the electrode. Diffusion of the gas phase is described [5, 20, 34] by the relation

$$J_g = \frac{D_g}{RT}\frac{dP}{dx}p \quad (3)$$

where D_g is the gas diffusion constant, dP/dx, replacing the concentration gradient, is the partial pressure

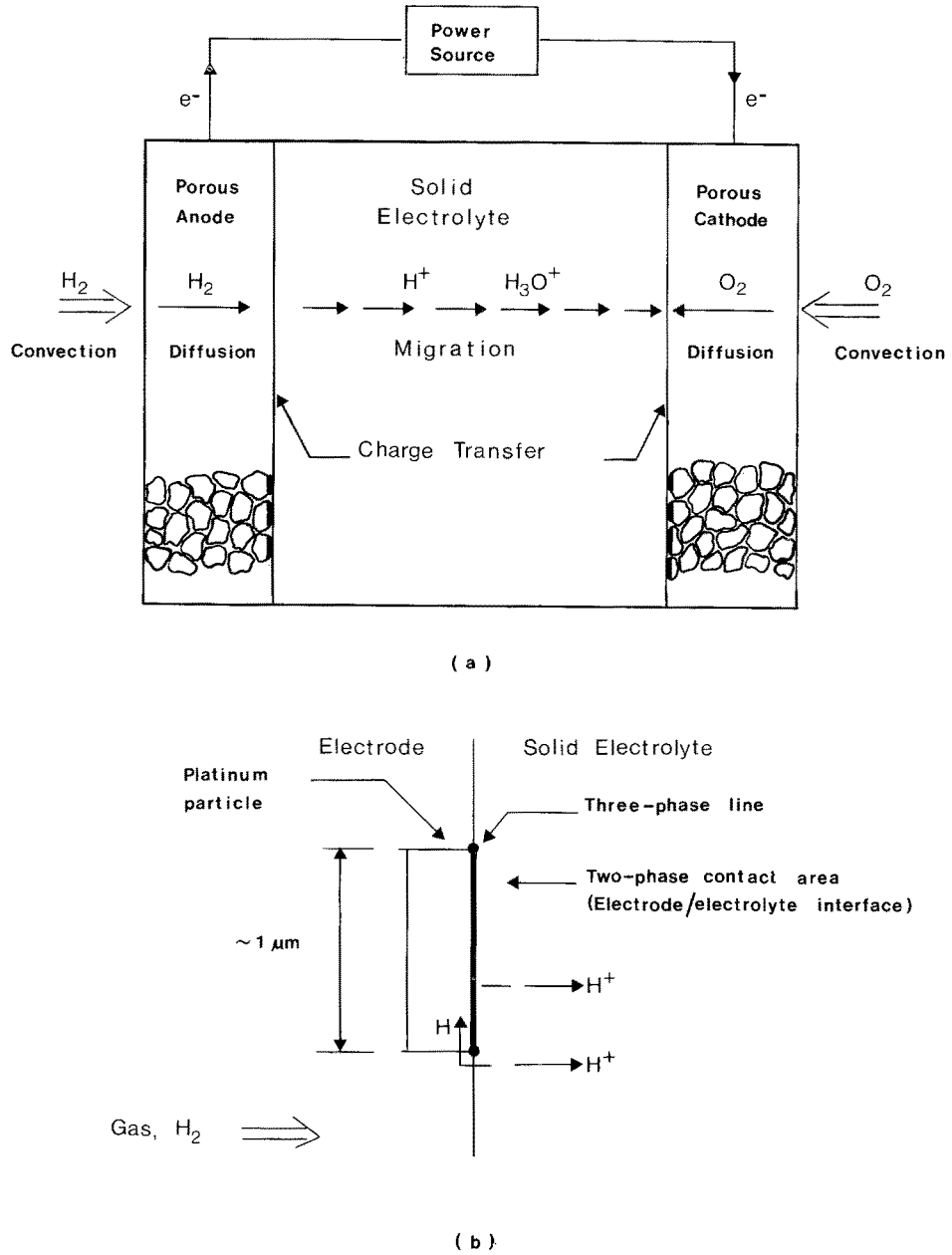

Figure 1 Schematic diagram of cell (a) with magnified view of interface (b).

gradient which is measured from the electrode's outer surface to the electrode–electrolyte interface, and p is porosity of the electrode. For self-diffusion of like molecules, the coefficient is given [34] by

$$D_{1,1} = \frac{\bar{v}\lambda_{1,1}}{3} \tag{4}$$

where $\bar{v}$ is the average molecular velocity assuming a Maxwell–Boltzmann distribution. The term, $\lambda_{1,1}$, is the mean free path between collisions of like molecules. For the interdiffusion of two different gas species, the coefficient, $D_{1,2}$, is used [34]. If the mean free path between collisions is larger than the pore radius, r, then Knudsen diffusion results in which the diffusion coefficient is given by

$$D_K = \tfrac{2}{3}\bar{v}r, \; r < \lambda \tag{5}$$

A second diffusional term is present when electrochemical species diffuse on the surface of the electrode or the electrolyte. This process has been considered [30] for diffusion along the three-phase line, L, according to the relation

$$J_s = D_s L \frac{dC}{dx} \tag{6}$$

where D_s is the surface diffusion coefficient. The electric current density for Equations 2, 3 and 6 is obtained from the relation

$$J = n_e F J_m$$

where n_e is the number of electric charges transferred during the electrochemical reaction, and J_m is the molar flux density. The migrational term of the electrolyte can also be written as Ohm's law

$$J = q\mu n E \tag{7}$$

in which q is the electric charge, μ is the mobility, n is the number density of the carriers, and E is the electric field or the voltage gradient, dV/dx.

In addition to convection, diffusion and migration, a charge-transfer mechanism occurs which is of the form $O + ne \rightleftharpoons R$. Here O represents the oxidized

species, ne is the number of electrons transferred, and R is the reduced species. This mechanism is modelled [27, 28] by the Butler–Volmer equation [30]

$$J_e = J_{o,e}\left[\exp\frac{(\alpha_a F_{\eta a})}{RT} - \exp\frac{(-\alpha_c F_{\eta c})}{RT}\right] \quad (8)$$

and occurs at the three-phase line and/or at the two-phase contact area. In this relation, $J_{o,e}$ is the exchange current density, α_a and α_c are the anodic and cathodic transfer coefficients; η_a and η_c are the anodic and cathodic overpotentials.

2.3. Polarization mechanisms

The operating voltage of an electrochemical cell, V_{cell}, is altered from its equilibrium or open-circuit value, V_{eq}, by polarization mechanisms, V_p, according [35] to the equation

$$V_{cell} = V_{eq} \pm V_p \quad (9)$$

The positive sign applies to externally driven cells, as in the case of electrolysis, and the negative sign is used for internally driven devices such as fuel cells.

Polarization mechanisms are a result of electrochemical process limitations; that is, slow processes (or low current densities) are manifested as large polarization voltages. Three mechanisms have been generally identified to occur in electrochemical cells. Concentration polarization results from a limitation of diffusing species either within the porous region of the electrode or at the interface. The term "ohmic polarization" has been applied to the migrational process of the electrolyte even though the polarization phenomena are more appropriately associated with the electrodes. The limitation due to the charge transfer process is known as activation polarization. The functional relations for these mechanisms are well known [35] and they combine to give a total cell polarization

$$V_p = V_{conc} + IR + V_{act} \quad (10)$$

where the term V_{conc} represents concentration polarization, IR is the ohmic loss of the electrolyte, and V_{act} is referred to as the activation polarization. Table I summarizes the various processes and polarization mechanisms as well as the controlling morphological parameters and possible measurement techniques.

3. Instrumentation

The conceptual and procedural aspects of each of the five measurement techniques as well as their adaptation to the analysis of film materials have been considered in detail [36] and will not be presented here. Image analysis was conducted with a LeMont Scientific OASYS system. A Rank Taylor Hobson Talysurf 6 profilometer was employed to measure the profilometry characteristics of the electrode surfaces. The gas permeability system was constructed by the Ontario Research Foundation. A Micromeritics Autopore 9200 porosimeter was used for mercury porosimetry measurements. For gas adsorption studies, a Micromeritics Orr Pore-Volume Surface-Area Analyser Model 2100 was utilized.

4. Results of film measurements

The first materials to be studied were platinum paste films because of their present use as electrodes for

TABLE I Electrochemical processes, polarization mechanisms, morphological parameters,and measurement techniques

Process	Polarization Mechanism	Controlling morphological parameter	Measurement technique
Convection	Concentration – if gas flow rate inadequate	None – gas flow is external to cell	Not applicable
	Concentration	Electrode thickness	
Gas diffusion of molecular species in porous region of electrode			Image analysis
		Porosity	Profilometry
		Pore size	Gas permeability
		Tortuosity	Mercury porosimetry
Self-diffusion, $r > \lambda$			Gas adsorption
Inter-diffusion, $r > \lambda$			
Knudsen diffusion, $r < \lambda$			
Surface diffusion of species on electrode	Concentration	Particle size	Image analysis
Surface diffusion of species on electrolyte	Concentration	Two-phase contact area	Image analysis
Surface diffusion of species along three-phase line	Concentration	Three-phase line	Image analysis
Charge transfer	Activation	Two-phase contact area	Image analysis
		Three-phase line	Image analysis
Catalytic activity	Not defined	Particle size	Image analysis
Heterogeneous catalysis	Capacitive effects appear as imaginary impedance components	Surface area	Mercury porosimetry Gas adsorption
Electrocatalysis	Ohmic	Two-phase contact area	Image analysis
Migration of ionic species through electrolyte		Electrolyte thickness	Profilometry for thin-film electrolyte

solid electrolytes. Plasma spraying as an electrode deposition method was examined by evaluating porous nickel films prepared by this process. Finally, a series of controlled-morphology silver-membrane filters were investigated.

4.1. Platinum paste films

The most common electrode material for solid-electrolyte cells is porous platinum. Pastes such as Engelhard 6926 or A-4338 have been developed specifically for oxygen-sensing applications in zirconia cells and are normally cured at ~800° C. These compositions have also been utilized for protonic electrolytes operating in the temperature range 25 to 300° C.

From Fig. 2 it can be seen that any pores which do exist within the platinum paste film are of the order of 1 μm diameter. Owing to the fine nature of these pores, regular epoxy mounting and polishing was unsuccessful in producing a cross-sectioned plane which had sufficient contrast between pores and particles. Viewed under the SEM, the polished samples appeared blurred and smeared such that no pore structure could be measured quantitatively.

In an effort to increase the contrast between particles and pores in the platinum film, a vacuum impregnation technique was employed. Unfortunately, this procedure did not result in any significant improvement for feature identification when viewed under the SEM. This result was due in part to the spatial resolution of the SEM which made it difficult to develop sufficient contrast between polished platinum particles suspended in a predominantly platinum background.

Examination of the polished platinum paste under an optical microscope, however, revealed that the platinum particles were indeed being polished to such a degree that they exhibited a marked contrast with the pores. Optical photomicrographs were measured through a camera/lens arrangement connected to the image analyser. The line-scan, lineal, and minimum-crossing-diameter (MCD) techniques resulted in similar values of particle size, pore size, and porosity.

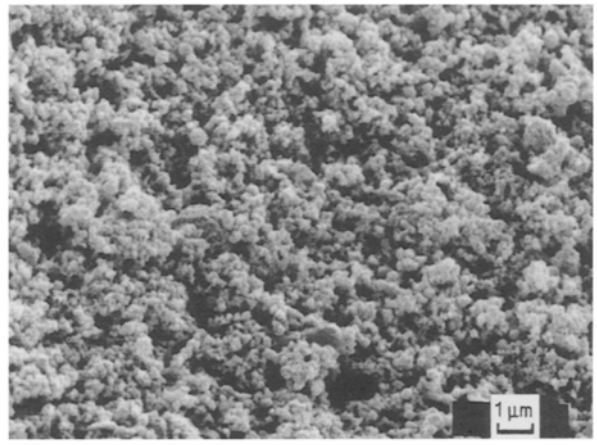

Figure 2 Scanning electron photomicrograph of A-4338 platinum paste cured at 100° C.

In Table II, the morphological parameters of the A-4338 platinum paste electrodes are compared with those of the 6082 platinum paste composition as well as with sputtered platinum electrodes. The thickness of paste electrodes is typically several micrometres, while that of sputtered layers is usually less than 1 μm. The porosity of both the paste and sputtered electrodes is widely variable and is dependent on composition, thermal treatment and applied current density. For the two cases where pore-size data are available, values for paste electrodes, 3 to 5 μm, are larger than those of sputtered layers, 0.5 to 1 μm. Particle sizes of paste layers are approximately 1 μm for both the A-4338 and 6082 compositions. The length of the three-phase line is approximately 5×10^3 cm cm^{-2} for sputtered layers. As a general rule, it can be seen that in the case of paste and sputtered electrodes applied to zirconia electrolytes, the morphological

TABLE II Morphological properties of platinum electrodes

Electrolyte type	Electrode composition	Deposition method	Treatment	Thickness (μm)	Porosity (%)	Pore size (m)	Particle size (m)	Three-phase line length (cm cm^{-2})	Reference
Bonded hydronium beta/beta″-alumina and Nasicon	Engelhard Pt paste A-4338	Brush	100° C hydrogen 1 h	10–40	65–72	3–5	2	5.5×10^3	[36]
Zirconia	Engelhard Pt paste 6082	Brush	600–100° C 30–300 mA	–	–	0.5–1	1	–	[35]
Zirconia	Engelhard Pt paste 6082	Brush	900° C at 100° C h^{-1}	–	30	–	1–2	5×10^3	[30]
Zirconia	Pt	Sputtered	1200–1400° C 1 V, 1 kHz 5 min	0.75	36	–	–	1.2×10^4	[29]
	Pt gauze	–	–	200 mesh/cm^2	36	–	–	1.4×10^1	
	Pt	Sputtered	973° C	0.3	1	–	$\leqslant 0.1$	$\geqslant 1.5 \times 10^5$	
	Pt	Sputtered	1173° C	0.3	7	–	0.5	3×10^4	
	Pt	Sputtered	1273° C	0.3	15	–	1.0	1.5×10^4	
Zirconia	Pt	Sputtered	750° C, 75 h	0.4	7	–	> 1	1.6×10^4	[27]
	Pt	Sputtered	900° C, 2 h	0.4	12	–	> 1	5.5×10^3	
	Pt	Sputtered	900° C, 50 h	0.4	48	–	> 1	7×10^3	

characteristics are quite similar. Furthermore, the properties of the Engelhard A-4338 platinum paste which was utilized with the bonded hydronium beta/beta″-alumina and Nasicon electrolytes are comparable to those measured for the zirconia electrodes. In addition to these morphological evaluations, the electrical resistance of the A-4338 composition as determined by two-probe measurements over a separation of 1 cm was found to be 5 to 10 Ω.

Preliminary profilometry work on the platinum films began by examining the surface texture of Engelhard ink no. 6926. Following SEM examination it was revealed that the bulk morphology of the films appeared to change with increasing firing temperature. To quantify this effect, small strips, approximately 3 mm × 15 mm were screen-printed on α-alumina substrates using the no. 6926 ink which had been diluted 3:2 with toluene (40%). The test specimens were cured in air at various temperatures ranging from abient (22° C) to 800° C. The surface textures of these films were measured together with their average thicknesses. From the values of centre-line average it was apparent that there was a significant increase in roughness with increasing temperature. There also appeared to be a striking change in film thickness for those pastes cured at $>400°$ C. These effects agree reasonably well with the SEM observations which showed the formation of a metallic coating for temperatures greater than 600° C. As the individual platinum particles sintered together to form interconnected islands, the porosity increased (thereby "roughening" the film) while the thickness decreased.

Gas permeability experiments were not conducted on platinum films due to the fragility of the material and problems associated with preparing the film on a well characterized porous substrate. A further difficulty in this approach was the penetration of the platinum ink into the porous substrate which caused an inaccurate measurement of permeability.

Owing to the limited thickness (10 to 40 μm) or the platinum paste films and to the prohibitive cost of successive layers, it was not possible to perform mercury porosimetry on these materials. An earlier work [38] examined the pore structure of insulating oxide films using electrical impedance measurements. Attempts to employ this method for the analysis of conductive platinum films were unsuccessful because of electrical instability.

Attempts were made to measure the surface area of A-4338 platinum paste using the Micromeritics Orr Pore-Volume Surface Area Analyser by increasing the absolute area present in the adsorption cell. Approximately 200 mm^2 (0.1 g) of hand-painted A-4338 paste (on glass slides) was introduced into the customized large adsorption cell for krypton analysis. This implied that the surface area of the film must be less than $\sim 3\ m^2\ g^{-1}$ when cured at 100° C (assuming a sensitivity of 0.01 $m^2\ g^{-1}$ and a total weight (slide and film of 300 g).

4.2. Plasma-sprayed nickel films

To study the effect of spray conditions (i.e. plasma power and/or working distance) and film thickness on reproducibility, a number of plasma coatings were prepared both in a supported and an unsupported manner. The supported films were prepared by spraying Metco powder 56C (nickel) on galvanized steel discs of approximately 2.5 cm diameter. The plasma conditions were Ar 6.87 × 10^5 Pa × 2.52 $m^3\ h^{-1}$, H_2 3.44 × 10^5 Pa × 0.283 $m^3\ h^{-1}$, 60 V, powder flow = 6 kg h^{-1}. The plasma current and working distance were then varied to produce seven coatings for each setting. The settings chosen were: Set 1, 500 A, 15 cm; Set 2, 300 A, 15 cm; and Set 3, 300 A, 25 cm. The thickness of these films as measured by optical microscopy ranges from 0.27 to 0.30 mm.

The unsupported films were prepared primarily for permeability measurements in which a free-standing film was necessary to eliminate any substrate effects on gas flow. These films were prepared by attempting to duplicate the plasma conditions and powder flow employed for the supported films. The substrates employed, however, were alumina discs of approximately 2.5 cm diameter. Previous experimentation indicated that if the α-alumina discs were roughened by grit blasting and preheated to remove excess and adsorbed moisture, then nickel could be bonded in a reasonable fashion to the ceramic substrate. If, however, the substrate was not pre-treated (both roughening and heating) then the plasma coatings did not display good bonding characteristics and could be easily removed.

Using this technique, a number of unsupported films of various thicknesses were prepared by increasing the number of passes of spray using a plasma current of 500 A and 15 cm working distance. Three sets were prepared as follows: Set 1, (1 × double pass), Set 2, (2 × double pass), and Set 3, (3 × double pass). Because each set varies only by the number of double passes, then thicknesses (and hence weights) are expected to increase proportionately.

Fig. 3 shows a typical optical photomicrograph of a representative field of view for samples analysed from the three sets of unsupported films. A qualitative assessment of these cross-sections indicated that they did indeed appear to be similar to the supported film of Set 1 which was produced using identical

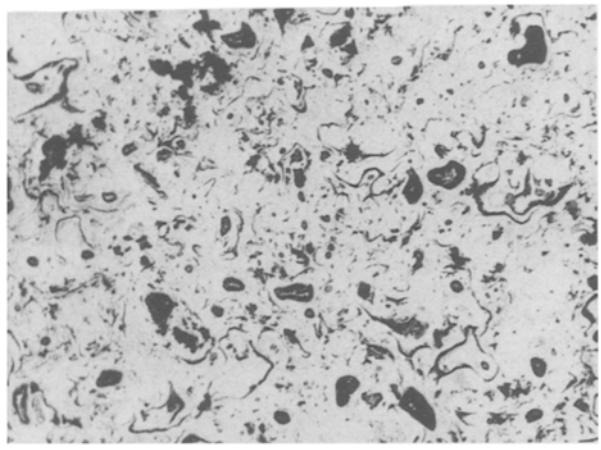

Figure 3 Optical photomicrograph of impregnated/polished plasma-sprayed unsupported nickel film (1 × double pass × 500 A, 6 in.) Mag. = 100×.

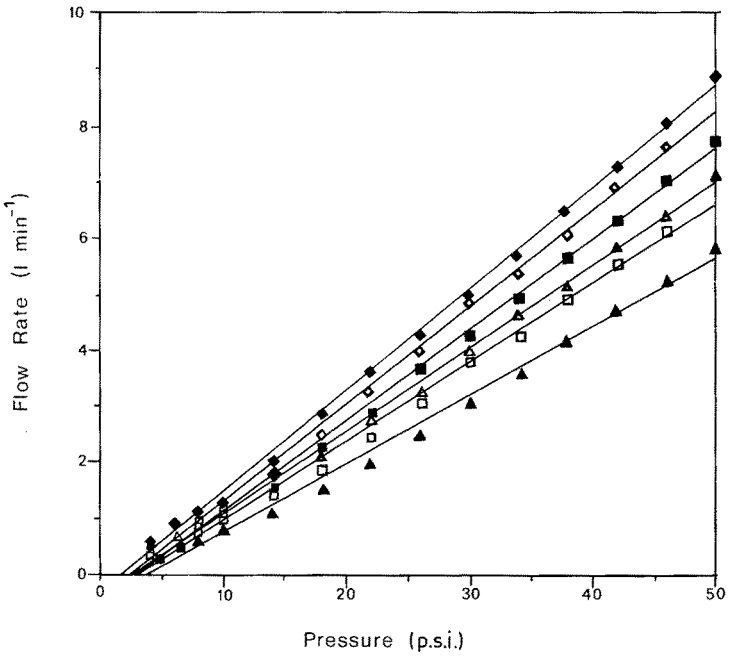

Figure 4 Permeability measurements of set 1 (single pass) unsupported nickel plasma-sprayed films. Samples: (◆) 1, 0.25 g; (◇) 3, 0.32 g; (■) 4, 0.32 g; (□) 5, 0.34 g; (▲) 2, 0.34 g; (△) 6, 0.35 g.

spray conditions (500 A, 15 cm working distance). Numerical evaluation by image analysis, however, revealed that there was no obvious trend for relating the "porous" structure to film thickness. Table III gives the morphological descriptors calculated from an extensive image analysis investigation on these unsupported films. These results indicate that although the thinnest and thickest films (Set 1 and Set 3, respectively) show excellent agreement in all categories, Set 2 appears significantly different in both particle size and porosity.

It was found that there was little difference between the surface texture of all three film types (within the standard deviations of the average values) which indicated that from a surface-texture point of view, increasing the film thickness in a plasma-spray operation had no effect on surface roughness.

In order to conduct permeability measurements on porous films, it was necessary either to support the film on a well-characterized porous substrate whose pore morphology was significantly larger than the test film (to avoid the support becoming the restrictive flow component) or to analyse totally unsupported films.

In this study, permeability measurements were used to evaluate the reproducibility of preparing porous electrodes using a plasma-spray technique as well as to define the effects of changing spray conditions (e.g. plasma power, working distance) on the overall pore morphology. These two conditions were extremely important when attempting to produce gas electrodes with identical and controlled morphologies.

In order to study the similarity of films produced under identical conditions, a number of porous nickel coatings were prepared by plasma spraying a non-roughened, non-preheated alumina disc of 25 mm diameter at standard conditions of 500 A and 15 cm spraying distance. Fig. 4 shows the observed flow/pressure curves for six films prepared by a single double pass of the automated spray gun. The film weights varied from 0.25 to 0.35 g which may have been related to the variability of the gravity feed flow system employed to introduce the nickel powder into the plasma. It is interesting to note, however, that the resistance to flow did not vary, in that a unique pore structure may be generated for each film. This behaviour may be expected because plasma spraying is a truly random process and the build-up of a film is determined by a variety of complex variables (e.g. powder size, flow, plasma temperature, position, etc.). The slopes of the flow curves ranged from 0.123 to 0.182 litre min p.s.i.)$^{-1}$ (10^3 p.s.i. ≡ 6.89 N mm^{-2}).

TABLE III Morphological properties obtained by image analysis for unsupported plasma-sprayed nickel films

Sample	IA technique	Morphological descriptor			
		Pore diameter (μm)	Particle diameter (μm)	Porosity (%)	Three-phase line (cm cm^{-2})
Set 1	Line scan (Area)	11.7	–	20.6 ± 4.4	450 ± 70
(1 × double pass)	Lineal	14.9	54.0	21.0	–
	MCD	19.4	60.1	–	–
Set 2	Line scan (Area)	10.2	–	15.2 ± 3.1	420 ± 70
(2 × double pass)	Lineal	12.6	71.1	14.3	–
	MCD	16.1	66.5	–	–
Set 3	Line scan (Area)	12.1	–	20.6 ± 5.1	450 ± 90
(3 × double pass)	Lineal	14.9	53.9	20.9	–
	MCD	20.1	60.3	–	–

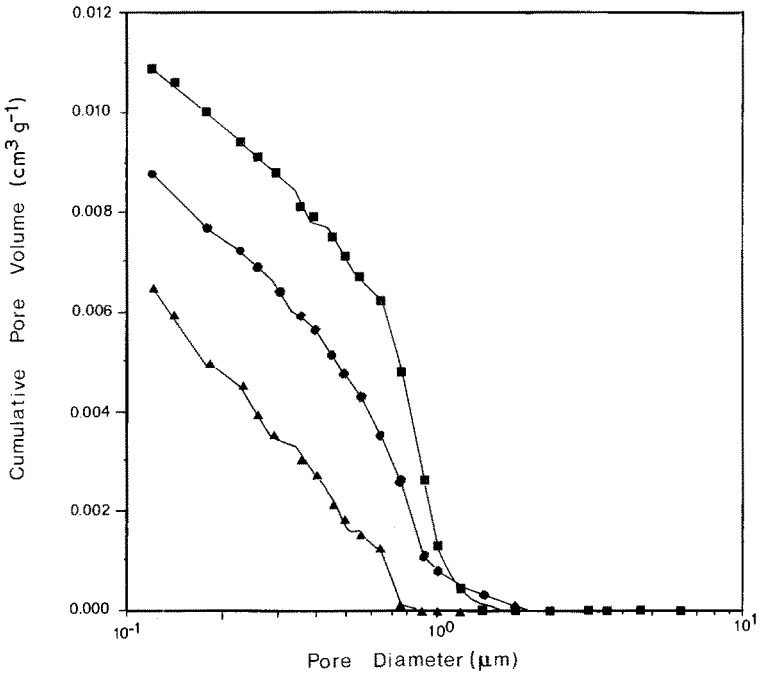

Figure 5 Mercury intrusion curves for unsupported nickel plasma films. (▲) Set 1, sample 4; (●) Set 2, sample 5, (■) Set 3, sample 1.

The application of mercury intrusion porosimetry is generally employed for the determination of porosity and pore-size distribution in samples with a relatively large void volume. The development of high-precision penetrometers during this study has enabled mercury porosimetry analysis to be extended by approximately one order of magnitude into the smaller sample volume end which allowed for the partial measurement of pore structure on individual plasma-sprayed films. Because it has been shown that the plasma-sprayed nickel coatings appear to be rather irreproducible with regard to pore morphology, the ability to measure and compare single films provided another opportunity to investigate the feasibility of the plasma-spraying process.

The three types of unsupported plasma-sprayed nickel coatings prepared using a different number of spray passes at 500 A and 15 cm were evaluated. Mercury intrusion porosimetry was conducted in the pressure range of 6.9×10^4 to 4.1×10^8 Pa (10 to 60 000 p.s.i.a.) using the Micromeritics AutoPore 9200 which resulted in a pore size range of 18 to 0.003 μm.

The cumulative intrusion curves showed the behaviour that at high pressures, mercury compression and other effects appear as sample intrusion. To avoid complicating the analysis, the pressure range of 2.1×10^5 to 1.0×10^7 Pa (30 to 1500 p.s.i.) was chosen, which corresponded to a pore size range of 6 to 0.12 μm. This selection omitted the extremely fine pores which were overlapped with compression effects and avoided the larger "pores" (i.e. intrusion between 20 and 10 μm) which were most likely due to the filling of surface irregularities.

From the intrusion curves, it appeared that there was an increase in the volume of pores of approximately 1 to 0.6 μm diameter as the number of passes increased. This effect, however, was complicated by the scaling factors employed. To isolate this effect more clearly, the intrusion volumes ($cm^3 g^{-1}$) for the range 6 to 0.12 μm were plotted in Fig. 5. From these curves, there appeared to be a trend that as the thickness of the film is increased there was a shift in pore size (to larger pores) and pore volume.

Each set was repeated (duplicate analysis) and the revised results at 2.1×10^5 to 1.0×10^7 Pa (30 to 1500 p.s.i.a.) are presented in Table IV. By averaging each of the two porosimetry runs, it was evident that there was, indeed, a trend towards higher porosity with increased film thickness. As the thickness was increased, the average pore diameter also appeared to increase. The pore area, however, remained relatively constant as the surface area for the volume (or number) of larger pores approximated the surface area of the smaller pores.

In an effort to obtain another measurement of porosity of these samples, the degree of mercury entrapment was monitored by recording the increase in weight for the samples following high-pressure intrusion. By assuming that the weight change was attributable to mercury being trapped in the pores of the sample, a volume was calculated (based upon the density of mercury) and related to the original sample volume by knowing the theoretical density of nickel ($8.90\,g\,cm^{-3}$) and the sample weight. These measurements are given in Table IV with the irregular porosimetry results. These results also indicated a trend towards higher porosities with increased film thickness.

When utilizing the gas adsorption method, it was necessary to increase the absolute surface area of the plasma-sprayed films under study by conducting a multiple-sample analysis using the large adsorption cells. Six sample sets were analysed corresponding to both the supported (various plasma conditions) and unsupported (thickness variation) films. Krypton adsorption was employed for the analyses and the results are summarized in Table V.

For the supported films, adsorption on the galvanized steel surfaces was assumed to be negligible due to its non-porous nature, and specific surface area estimates relate to the film weight only. From these

TABLE IV Mercury porosimetry analysis of unsupported plasma-sprayed nickel films (500 A, 15 cm)

Parameter	Set 1 (1 × double pass)		Set 2 (2 × double pass)		Set 3 (3 × double pass)	
	Sample 4	Sample 6	Sample 6	Sample 5	Sample 1	Sample 2
Intrusion volume ($cm^3 g^{-1}$) (30 – 1500 p.s.i.a.)	0.0065	0.0018	0.0077	0.0088	0.0109	0.0074
Pore area ($m^2 g^{-1}$) (30 – 1500 p.s.i.a.)	0.094	0.031	0.089	0.092	0.097	0.081
Average pore diameter (μm) (30 – 1500 p.s.i.a.)	0.28	0.23	0.35	0.38	0.45	0.37
% Porosity (30 – 500 p.s.i.a.)	5.5	1.6	6.4	7.3	8.8	6.2
Average % porosity	3.6 ± 2.8		6.8 ± 0.6		7.5 ± 1.8	
Mercury entrapped (ml)	0.0026	0.0029	0.0069	0.0056	0.0105	0.0114
Weight sample (g)	0.32	0.35	0.71	0.58	1.01	1.07
% Porosity	6.7	6.9	8.0	7.9	8.5	8.7
Average % porosity	6.8 ± 0.1		7.9 ± 0.1		8.6 ± 0.1	

results, it appeared that there was little significant difference between the films analysed, with the possible exception of the unsupported three double-pass samples (Set 3). One possible explanation of this result is that with increased working distance the molten droplets have a better opportunity to cool, thereby destroying some microstructural features (e.g. nanopores) which would give rise to an increased surface area. The pore area of approximately $0.07 m^2 g^{-1}$ as determined by mercury porosimetry is in good agreement with the surface area of 0.05 to $0.08 m^2 g^{-1}$ resulting from gas adsorption analysis.

4.3. Silver membranes

Silver membrane filters [39] were also used to evaluate the various characterization techniques. These metal membranes offered the advantages of relative uniformity, controlled porosity, pore retention rating (ranging from 5 to 0.2 μm), and an approximation to the physical dimensions of other electrode materials which were studied (e.g. thicknesses of 40 to 70 μm).

Fig. 6 shows the virgin surface of a 5 μm filter and demonstrates the morphological nature of these silver membrane filters. The proprietory manufacturing process appeared to be a result of a powder sintering action, possibly in conjunction with a volatile organic pore former. The result was a very porous and tortuous structure with well-defined particle retentive abilities.

Five silver membrane pore ratings (5.0, 1.2, 0.80, 0.45 and 0.20 μm) were selected for detailed quantitative image analysis. In each case, a 25 mm diameter membrane was prepared by mounting the specimen in standard metallurgical epoxy followed by grinding and polishing it down to the minimum of a 1 μm diamond paste finish. Polished samples were either gold coated for subsequent SEM examination or in some cases (for pore ratings greater than 0.5 μm) analysed directly by optical microscopy techniques. In both situations, it was necessary to treat or analyse the samples immediately to avoid oxidation of the exposed silver metal which distorted the pore structure image.

TABLE V Surface area of plasma-sprayed nickel films and silver membrane filters

(a) Plasma-sprayed nickel films

Substrate	Spray conditions	Specific surface area ($m^2 g^{-1}$)
Galvanized steel	500 A, 15 cm	0.075 ± 0.007
Galvanized steel	300 A, 15 cm	0.064 ± 0.005
Galvanized steel	300 A, 15 cm	0.067 ± 0.006
Unsupported	500 A, 15 cm 1 × double pass	0.070 ± 0.003
Unsupported	500 A, 15 cm 2 × double pass	0.065 ± 0.001
Unsupported	500 A, 15 cm 3 × double pass	0.048 ± 0.004

(b) Silver membrane filters

Particle retention rating (μm)	Specific surface area ($m^2 g^{-1}$)	Volumetric surface* area ($cm^2 cm^{-3}$)	Stereological† surface area estimate ($cm^2 cm^{-3}$)
1.2	0.0160	7900	6400
0.8	0.0132	6500	6400
0.45	0.0132	9500	6200
0.2	0.0113	7750	6100

*Based upon thickness values measured by profilometry (see table).
†From image analysis measurement of the three-phase line.

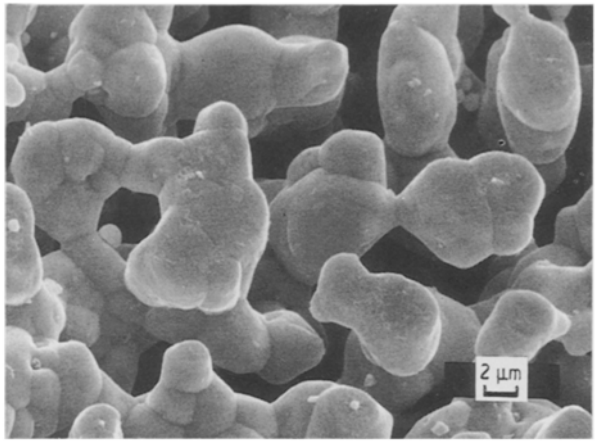

Figure 6 Scanning electron photomicrograph of 5 μm rated silver membrane surface.

Table VI gives the mean particle/pore diameter measured by a chord length distribution analysis. In each case, seven to ten frames (photomicrographs) were analysed with five lines per frame corresponding to between 250 and 500 individual feature measurements. As can be seen from this table, the particle diameters remained relatively constant while the pore diameters decrease in size. There existed a very good correlation between the pore diameters measured by the lineal approach and the minimum crossing distance (MCD) technique developed specifically for evaluating porous structures. Table VI also shows the measured average particle diameter using the line scan or area equivalent diameter logic. As with the chord length of line scan analysis, the particle diameters remained relatively constant until the silver particulates became the continuous phase (i.e. pore rating $< 0.5\,\mu$m) whereupon the measured particle diameters became exaggerated.

The decrease in pore diameter while maintaining a consistent particle diameter resulted in a decrease in overall porosity. As with the feature dimension analysis, the porosities of the silver membranes can be measured in a number of ways. Table VI lists the per cent porosity for each polished membrane filter using both a line scan (area) technique and a chord length to total length analysis (both voids and particles). From this table, it is apparent that for porous silver membranes with less than approximately 30% porosity, the solid phase becomes continuous.

One other important parameter that can be derived from image analysis is the perimeter-to-area ratio for selected features (either pores or particles). If one were able to examine particles of the electrode situated at the electrolyte (i.e. interface), this perimeter would correspond to the three-phase line. It can be assumed that if a porous body has a random yet uniform structure, such as the silver membranes, then any cross-sectioned plane should approximate any other and hence the three-phase line calculated on any section would be an estimate of the value at the interface. Except for the 5 μm membrane, all the filters exhibited a three-phase line of approximately 6300 cm cm^{-2}; the 5 μm membrane had a value of 3400 cm cm^{-2}. This is somewhat expected because, as was shown earlier, the particles remained relatively constant in size while the porosity decreases to account for a smaller pore dimension. Overall, however, the particle perimeter per unit area did not change significantly.

Using the profilometry method, investigations were begun by measuring the surface roughness of virgin surfaces for the five silver membranes under study. Samples were mounted on a vacuum-holding device. Ten traces were acquired on each membrane using the skidless, standard styles (approximately 2 μm tip radius) and using the phase-corrected mode at a sampling length of 0.08 mm. The small sampling length was chosen to avoid problems in sample levelling which often become dominant when operating in a skidless mode.

It was apparent that there existed a strong correlation between virgin surface texture and particle retention rating for the silver membranes. This effect was most likely attributable to the physical dimensions of the pore diameters. However, it was also complicated by the fact that by using the standard stylus tip, smaller irregularities (e.g. pores) could have been under-detected leading to the interpretation of a smoother surface.

Profilometry was also used to study the thickness and uniformity of the membranes. In an effort to cross-correlate the porosity measurements observed through image analysis, four silver membrane types were selected for volumetric/gravimetric determination of porosity. Three fresh individual samples of each membrane material were mounted on the vacuum holder such that the filter edge could be easily measured. A minimum of five edges per membrane were measured to provide a reasonably accurate estimate (and standard deviation) for membrane thickness. From this thickness measurement, and by knowing the membrane area (25 mm diameter), a total volume could be computed. This volume was then related to the actual mean weight of a membrane and by using the specific gravity of pure silver (10.5 g cm^{-3}), a porosity value could be obtained.

Table VII lists the measured dimensions and weights as well as the calculated porosity. The porosity values agreed reasonably well with those shown see Table VI. The observed deviations were most likely due to the variance in measuring the membrane thickness and weight.

The five particle retention-rated silver membranes were measured for gas flow against pressure head using helium. These data showed excellent fits for the five materials, all of which correspond to the behaviour displayed by other filter membranes (e.g. Nuclepore [40] and Millipore [41]). Only the 0.2 μm membrane was either sufficiently non-porous or with fine enough pore diameter to produce any significant change in the flow/pressure curve from the blank run.

The 0.2 μm membrane was subsequently selected for investigation of its flow/pressure characteristics using the reactant gases for the "model" fuel cell, hydrogen and oxygen. Fig. 7 shows the measured flow curves for the same flowmeter setting. The needle valve into the rotameter tube acted as a flow resistor which limited the gas passage for the various gases.

TABLE VI Pore diameters, particle diameters and porosity as determined by image analysis for silver membranes

Pore diameter			Particle diameter		Porosity (%)		
Pore rating (μm)	Minimum crossing distance (μm)	Ave. chord length (μm)	Line scan area (μm)	Ave. chord length (μm)	Area Determinations	Chord length (particles)	Chord length (voids)
5.0	3.2	4.3	5.9	4.8	44 $\pm$ 9	47	47
1.2	2.2	2.5	5.8	2.7	47 $\pm$ 4	48	48
0.8	1.5	1.9	4.9	3.4	34 $\pm$ 2	35	35
0.45	1.2	1.2	7.6	3.6	24 $\pm$ 6	26	24
0.2	1.0	1.0	8.5	4.0	20 $\pm$ 2	20	20

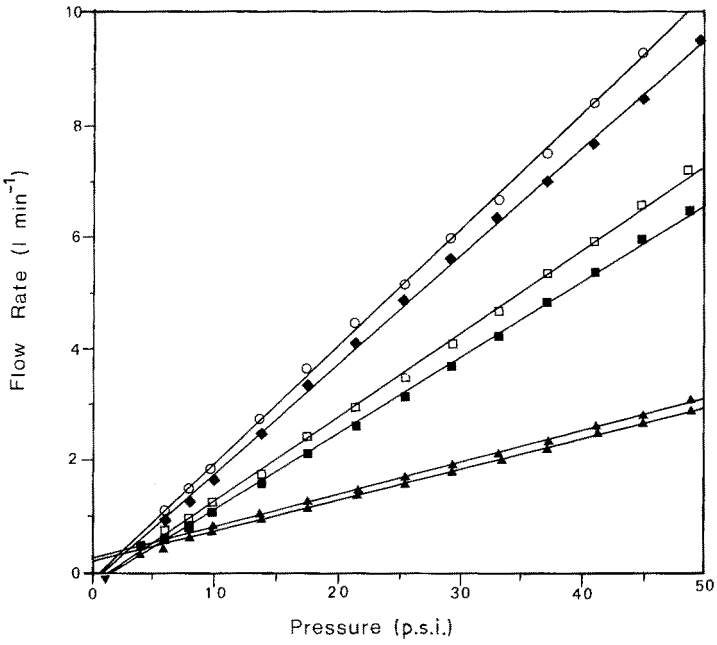

Figure 7 Comparison of permeability for 0.2 μm silver membrane with different gases. (□) Blank (He); (■) 0.2 AG (He); (○) blank (H_2); (◆) 0.2 AG (H_2), (△) blank (O_2); (▲) 0.2 AG (O_2).

This had the effect of lowering gas flow through the rotameter, depending upon gas composition. The slopes of the flow curves are proportional to the mean free paths of the gas which for oxygen, hydrogen, and helium are 0.099, 0.174 and 0.275 μm, respectively at 20° C and 75 cm Hg [42]. Thus, from Equations 3 and 4, the diffusion constant and the current density will be larger for hydrogen than for oxygen if the gas pressure gradient and film porosity are the same.

Because of the formation of a silver–mercury amalgam, it was not possible to conduct a mercury-porosimetry analysis on the silver membranes. Future developments into the area of Wood's metal porosimetry (bismuth–lead–tin–cadmium compounds) may prove to be useful not only in conducting standard high-pressure intrusion analysis but in the physical characterization of porous bodies by "freezing" the Wood's metal in the pores and then examining the pore shape by SEM/optical image analysis techniques.

Owing to the small absolute surface area of each individual membrane and the limit of sensitivity of the Micromeritics Orr Pore-Volume Surface-Area Analyser Model 2100, it was necessary to increase the sample volume by measuring twenty membranes in unison. Table IV gives the specific surface areas measured as well as the surface area per unit volume ($cm^2\ cm^{-3}$) of membrane material. The 5 μm membrane was not measured due to the unavailability of twenty virgin samples. Table IV also lists the estimate of surface area based upon the stereological measurement of the three-phase line (or perimeter) by image analysis. Although the agreement between the BET technique and image analysis is not as good as one would expect, the values are of the same order of magnitude and agree to within 35%. Possible deviations would be expected due to the inability of the image analysis technique to measure minute crevices or pores which would certainly be accessible by Krypton gas adsorption, resulting in an increase in surface area.

5. Conclusions

The purpose of this study has been to identify, test, and refine characterization techniques for the physical examination of film morphologies. The five techniques selected in this study for detailed evaluation have all been shown to be capable of producing film morphological data, provided certain restrictions regarding material types, preparative methods, and the absolute sensitivity of the instruments employed are considered. The interpretation and cross-correlation of these data was made rather complicated by film irreproducibility and by the destructive nature of some of the techniques (e.g. mercury porosimetry and impregnation for image analysis). As a result, it was necessary to assess each technique with regard to its practicality (i.e. advantages/disadvantages) in producing reliable information which could be employed to measure the physical properties of porous electrode structures.

Image analysis is considered to be the most versatile method currently available for studying film morphology. This technique has been shown to provide data on all the physical properties which are considered relevant to electrochemical behaviour (i.e. pore size, particle size, pore/particle interface length,

TABLE VII Gravimetric/volumetric determination of porosity for silver membranes

Absolute particle retention (μm)	Weight (g/membrane)	Thickness (μm)	Porosity (%)
1.2	0.126 ± 0.009	52 ± 4	53
0.8	0.170	70 ± 4	53
0.45	0.180	51 ± 5	32
0.2	0.126	37 ± 2	34

and total porosity and three-phase-line length). The sensitivity of image analysis is limited only by the ability to produce input images of sufficient contrast and resolution. The size of features is generally not considered to be a limitation because atomic-level discrimation can be achieved with state-of-the-art transmission electron microscopy imaging. The primary limitation of image analysis, as seen in this study, is the difficulty in producing an image which adequately differentiates pores and solids. In materials of simple composition and semi-regular pore structure, such as the silver membranes standard preparative methods such as epoxy impregnation were found suitable for developing this discrimination. In films with multi-phase components (e.g. oxides in metal plasma films, organics in platinum pastes) or microporosity (either low porosity or extremely fine pores), other preparative methods or even alternative image forming techniques (e.g. acoustic microscopy) may be necessary.

Although profilometry makes possible the generation of physical data on film materials in a non-destructive, rapid manner and without the need for involved sample preparation, its application to the direct investigation of bulk film morphology must be viewed in consideration of a number of effects. Profilometry examines surface effects only and is generally applied to the interaction of surfaces with other materials (e.g. bearing ratios, corrosion, erosion). On a macroscopic scale, gross deviations in the surface are indeed related to the bulk (e.g. "swiss-cheese") morphology; however, on a microscopic scale, physical forces involved in the formation of a surface may distort the interface such that it does not represent or "mirror" the porous structure contained below. This disparity is particularly evident for films which are formed by methods involving a high degree of surface interaction (e.g. pressing and painting).

The gas-permeability method offers the simplest means of evaluating a film's total porous nature. Relative differences in the film's physical properties (i.e. thickness, pore-size distribution, per cent porosity) are easily differentiated with regard to which material and unique morphology can pass a particular volume of a specific gas per unit time. This result has obvious consequences when relating the permeability of porous electrodes to the behaviour of electrochemical devices and provides a direct measurement of a film's suitability in this area. In order to conduct permeability measurements, it is necessary to study unsupported films or films which are supported on a well-characterized and highly reproducible substrate. This restriction affects the application of the technique for the measurement of gas flow properties of an electrode directly because most electrolytes (substrates) commonly employed are non-porous and non-permeable. As a result, the films evaluated by permeametry in this study were of a free-standing nature and no porous substrates were employed. The results have indicated that permeability measurements are particularly useful for studying the variables in producing porous coatings (e.g. plasma films) and for evaluating film reproducibility. Permeametry has therefore been shown to be best applied in a secondary manner for studying the deposition conditions and reproducibility involved in film production as opposed to measuring actual electrode morphological features.

Traditional mercury intrusion porosimetry using conventional equipment has been shown to have rather limited applications when applied to electrode films. The primary limitation of this method is the total sample volume which must be of sufficient quantity to permit detection of the intruded mercury. For the customized penetrometers developed as part of this study, the technique has been shown to be suitable when applied to single films approximately 50 μm or greater in thickness with porosities in excess of approximately 5%. Although the sample volume can be increased by adding more samples, this procedure has the effect of "averaging" results over large populations which may not be desirable if one is interested in film variability. The technique employed in this study has been shown to be restricted in pore range due to problems resulting from the more sensitive penetrometers. The lower pore size value is presently limited to about 0.1 μm. Mercury porosimetry was found to be a destructive technique, dependent on pore shape and tortuosity. For the plasma-sprayed nickel films, this method was affected by surface texture. It is also limited by the formation of silver and gold amalgams. The technique does not distinguish between different portions of the sample which means that films are best analysed when they are unsupported or that the supports must be smooth and non-porous (e.g. glass or metal) in order to avoid affecting the intrusion curves. Overall, mercury porosimetry cannot be viewed as a practical means of assessing film morphology until alternative methods can be implemented for increasing the sensitivity of measuring the intrusion of mercury into the pores. Although preliminary attempts to make impedence-porosimetry measurements did not result in a usable technique, further study in this area could result in an improved technique for characterizing physical structures.

As was the case for conventional mercury porosimetry, gas adsorption has been found to be limited by sample size. Through specially designed cells, it has been possible to extend the sensitivity of this technique down to 0.1 $m^2 g^{-1}$. New commercial instrumentation is capable of measuring down to 0.01 $m^2 g^{-1}$. However, in order to meet the demands of most film applications, where only small amounts of material (e.g. milligrams) are present, a high vacuum system employing ultra-sensitive detection equipment will be necessary. By increasing the number of samples, and therefore the sample volume, it has been possible to increase the instrumental sensitivity.

Although the anodic (hydrogen) electrode polarization mechanisms can be neglected for the ZrO_2 and $SrCeO_3$ cells operating in the temperature range of 800 to 1000° C, the activation and concentration phenomena occurring here will significantly affect the protonic cells which operate at 25 to 300° C. When oxygen is present at the cathode in the full-cell mode, its polarization will also limit the cell performance for both the anionic and the cationic electrolytes. Thus, an under-

standing of the morphological parameters of both electrodes and their relation to the polarizations processes will be essential for the improved utilization of solid electrolytes. It is evident that the techniques described here will be of value in the determination of these parameters and in the further development of electrodes for solid electrolytes.

References

1. C. S. TEDMON, H. S. SPACIL and S. P. MITOFF, *J. Electrochem. Soc.* **116** (1969) 1170.
2. H. YANAGIDA, R. J. BROOK and F. A. KROGER, *ibid.* **117** (1970) 593.
3. T. H. ETSELL and S. N. FLENGAS, *ibid.* **118** (1971) 1890.
4. R. J. BROOK, W. L. PELZMANN and F. A. KROGER, *ibid.* **118** (1971) 185.
5. S. PIZZINI, M. BIANCHI, P. COLOMBO and S. TORCHIO, *J. Appl. Electrochem.* **3** (1973) 153.
6. C. MARI, V. SCOLAIR, G. FIORI and S. PIZZINI, *ibid.* **7** (1977) 95.
7. T. GUR, I. D. RAISTRICK and R. A. HUGGINS, *J. Electrochem. Soc.* **127** (1980) 2620.
8. J. MIZUSAKI, K. AMANO, S. YAMAUCHI and K. FUEKI, *Solid State Ionics* **22** (1987) 313.
9. *Idem, ibid.* **22** (1987) 323.
10. H. UCHIDA, N. MAEDA and H. IWAHARA, *J. Appl. Electrochem.* **12** (1982) 645.
11. H. IWAHARA, H. UCHIDA and N. MAEDA, *Solid State Ionics* **11** (1983) 109.
12. H. IWAHARA, H. UCHIDA and S. TANAKA, *ibid.* **9/10** (1983) 1021.
13. H. UCHIDA, S. TANAKA and H. IWAHARA, *J. Appl. Electrochem.* **15** (1985) 93.
14. A. AHMAD, T. A. WHEAT, A. K. KURIAKOSE and J. D. CANADAY, Presented at the Electrochemical Society Fall Meeting, New Orleans, Louisiana, October 1984, Division Report ERP/MSL 84-93 (OP&J) (CANMET, Energy, Mines and Resources Canada, 1984).
15. A. K. KURIAKOSE, T. A. WHEAT, A. AHMAD and J. D. CANADAY, Presented at the Annual Meeting of the Canadian Ceramic Society, Ottawa, Ontario, February 1985; Division Report ERP/MSL 85-26 (OP) (CANMET, Energy, Mines and Resources Canada, 1985).
16. *Idem, J. Solid State Chemistry* **69** (1987) 312.
17. A. K. KURIAKOSE, T. A. WHEAT, A. AHMAD and J. DIROCCO, *Amer. Ceram. Soc.* **67** (3) (1984) 179.
18. A. AHMAD, T. A. WHEAT, A. K. KURIAKOSE and J. D. CANADAY, Presented at the Annual Meeting of the Canadian Ceramic Society, Ottawa, Ontario, February 1985; Division Report, ERP/MSL 85-22 (OP) (CANMET, Energy, Mines and Resources, Canada, 1985).
19. A. K. KURIAKOSE, T. A. WHEAT, A. AHMAD, J. D. CANADAY and A. J. HANSON, Canadian Pat. Application 4 859 464, June 28 1985.
20. J. JENSON and M. KLEITZ, "Solid State Protonic Conductors I" (Odense University Press, Odense, Denmark, 1982).
21. J. B. GOODENOUGH, J. JENSEN and N. KLEITZ, "Solid State Protonic Conductors II" (Odense University Press, Odense, Denmark, 1983).
22. *Idem*, "Solid State Protonic Conductors III" (Odense University Press, Odense, Denmark, 1985).
23. J. D. CANADAY, A. K. KURIAKOSE, A. AHMAD and T. A. WHEAT, *J. Canad. Ceram. Soc.* **55** (1986) 34.
24. J. GULENS, T. H. LONGHURST, A. K. KURIAKOSE and J. D. CANADAY, Presented at the Sixth International Conference on Solid State Ionics (1987), and *Solid State Ionics* **28/30** (1988) 622.
25. J. D. CANADAY, A. K. KURIAKOSE, T. A. WHEAT and A. AHMAD, Division Report ERP/MSL 86-156 (IR) (CANMET, Energy, Mines and Resources Canada, 1986).
26. M. Z. MUNSHI and P. S. NICHOLSON, *Solid State Ionics* **23** (1987) 203.
27. S. P. S. BADWAL and F. T. CIACHI, *ibid.* **18/19** (1986) 1054.
28. D. Y. WANG and A. S. NOWICK, *J. Electrochem. Soc.* **126** (1979) 1155.
29. M. J. VERKERK, M. W. J. HAMMINK and A. J. BURGGRAAF, *ibid.* **130** (1983) 70.
30. D. BRAUNSHTEIN, D. S. TANNHAUSER and I. RIESS, *ibid.* **128** (1981) 82.
31. J. O. M. BOCKRIS and A. K. N. REDDY, "Modern Electrochemistry", Vol. 2 (Plenum, New York, 1970).
32. D. Y. WANG and A. S. NOWICK, *J. Electrochem. Soc.* **128** (1981) 55.
33. A. J. BARD and L. R. FAULKNER, "Electrochemical Methods" (Wiley, New York, 1980).
34. J. D. CANADAY, T. A. WHEAT, A. AHMAD and A. K. KURIAKOSE, *J. Appl. Electrochem.* **17** (1987) 545.
35. J. D. CANADAY, T. A. WHEAT, A. K. KURIAKOSE and A. AHMAD, *Int. J. Hydrogen Energy* **12** (3) (1987) 151.
36. M. P. HALEY, DSS File No. 03SQ.23440-4-9223 (CANMET, Energy Mines and Resources, Canada, 1987).
37. Engelhard Corporation, Speciality Chemicals Division, 1 West Central Avenue, East Newark, New Jersey 07029 (1989).
38. B. COX, *J. Nucl. Mater.* **27** (1968) 1.
39. Osmonics, Inc., 5951 Clearwater Drive, Minnetonka, Minnesota 55343 (1987).
40. Nuclepore Corporation of Canada, 30 Fordhouse Boulevard, Toronto, Ontario, Canada M8Z 5M3 (1987).
41. Millipore Limited, 3688 Nashua Drive, Mississauga, Ontario, Canada L4V 1M5 (1987).
42. R. C. Weast (Ed.), CRC Hand book of Chemistry and Physics, 63rd Edn (CRC Press, Cleveland, Ohio, 1982).

Received 13 January 1988
and accepted 14 February 1989